Budding and domain shape transformations in mixed lipid films and bilayer membranes

J. L. Harden*
Department of Chemical Engineering, Johns Hopkins University, Baltimore, Maryland 21218-2689, USA

F. C. MacKintosh†
Division of Physics & Astronomy, Vrije Universiteit, 1081 HV Amsterdam, The Netherlands

P. D. Olmsted‡
School of Physics & Astronomy and Polymer IRC, University of Leeds, Leeds LS2 9JT, United Kingdom
(Received 10 November 2004; published 5 July 2005)

We study the stability and shapes of domains with spontaneous curvature in fluid films and membranes, embedded in a surrounding membrane with zero spontaneous curvature. These domains can result from the inclusion of an impurity in a fluid membrane or from phase separation within the membrane. We show that for small but finite line and surface tensions and for finite spontaneous curvatures, an equilibrium phase of protruding circular domains is obtained at low impurity concentrations. At higher concentrations, we predict a transition from circular domains, or *caplets*, to stripes. In both cases, we calculate the shapes of these domains within the Monge representation for the membrane shape. With increasing line tension, we show numerically that there is a budding transformation from stable protruding circular domains to spherical buds. We calculate the full phase diagram and demonstrate two triple points of, respectively, bud-flat-caplet and flat-stripe-caplet coexistence.

DOI: 10.1103/PhysRevE.72.011903 PACS number(s): 87.16.Dg, 68.05.−n, 68.18.Jk

I. INTRODUCTION

Fluid membranes occur in a wide variety of physical, chemical, and biological systems [1–4]. Examples include surfactant films, unilamellar and multilamellar vesicles, and lipid bilayer membranes, such as those in biological cells. Increased attention has been paid to the properties of multicomponent bilayer membranes. There are at least two important reasons for this. On the one hand, biological cell membranes naturally involve mixtures of several different lipid and protein components [3,4]. Processes such as budding, shape, and textural transformations and raft formation are believed to involve local inhomogeneities in these mixtures [5–17]. On the other hand, lipid mixtures have been shown to play an important role in the formation of stable vesicles for a variety of potential biomedical applications such as controlled gene and drug delivery [18,19].

The additional internal degrees of freedom that accompany the presence of two or more components within a fluid membrane can lead to a rich set of different membrane properties. The understanding of the effects of composition variations on membrane properties is important, as it may shed light on the behavior of cell membranes and also enable rational control of synthetic membrane structure and function. The compositional degrees of freedom in a multicomponent membrane can dramatically influence both its morphology and phase behavior. For instance, phase separation within the membrane can occur, analogous to phase separation of ordinary fluids. However, such two-dimensional phase separation within a membrane is expected to be closely linked to the three-dimensional shape of the membrane. This is because, at a microscopic level, the curvature properties, and especially the spontaneous curvature, are largely dictated by the structure of the constituent molecules [20]. Thus, regions of different composition will often have different curvature properties. In such cases, the formation of a domain of one phase within a matrix of another phase can lead to a localized deformation of the membrane. This deformation can be enhanced by finite line tension between domains, which when sufficiently large can drive budding (the formation and subsequent separation of a small vesicle). Experimental studies of model two- and three-component systems have examined domain formation [5,7–14] and its role in the process of membrane shape transformations [11,12] and budding [5,7].

Many theoretical studies have examined the interplay between internal degrees of freedom and membrane shape in two-component fluid membranes [21–35]. In theoretical studies of phase-separated bilayer vesicles, it was found that budding can occur in the limit of large line tension between the two phases [28,29,33]. However, when surface tension is relevant, phase separation can lead to stable, modulated phases of flat films and vesicles [22,25–27,32–35]. Indeed, equilibrium-modulated morphologies have been observed in several recent studies of phase-separated multicomponent bilayer vesicles [11,12]. On the other hand, the deformation of homogeneously mixed two-component fluid membranes may induce in-plane phase separation [30].

For a mixed monolayer, the deformation of the film due to phase separation of two components with differing spontaneous curvature is an immediate consequence of the different molecular architectures of the two components. For a bilayer membrane, however, the coupling of composition to curva-

*Electronic address: harden@jhu.edu
†Electronic address: fcm@nat.vu.nl
‡Electronic address: p.d.olmsted@leeds.ac.uk

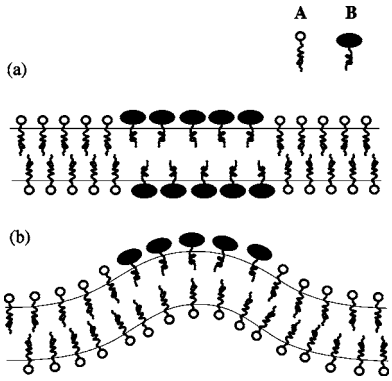

FIG. 1. (a) Flat symmetric phase-separated membrane and (b) curved, asymmetric phase-separated membrane.

ture is somewhat more subtle because of symmetry considerations. Phase separation can take two different forms within a bilayer membrane. As shown in Fig. 1(a), a symmetric domain of one component can develop within a matrix of another phase. In Fig. 1(b), an asymmetric domain is shown, in which the two halves of the bilayer have different compositions. As illustrated in the figure, these effects can influence the shapes and phase behavior of membranes in different ways. In the symmetric case [Fig. 1(a)], the domain can remain flat [28], although the domain can be more or less rigid than the surrounding membrane, a situation reminiscent of rafts in biological membranes. However, composition inhomogeneities can give rise to deformation of a bilayer membrane if there is an asymmetric distribution of the lipid constituents across the bilayer, as shown in Fig. 1(b) [36]. Such lipid asymmetry has been clearly demonstrated experimentally in biological membranes [37,38]. This broken symmetry of the bilayer can either arise spontaneously [31] or as a result of different environments on the inside and outside of a vesicle. In the latter case, we must also consider the possibility of a nonzero surface tension due to an osmotic pressure difference between the inside and outside.

In this paper, we examine the stability and equilibrium shapes of domains in asymptotically flat fluid films (or giant vesicles with dimensions much larger than the domain sizes). We focus on domains of constituents with finite effective spontaneous curvature, embedded in a matrix of membrane material with zero spontaneous curvature. These domains can either be due to phase separation of two or more components in a mixed membrane or to the inclusion of an "impurity" in the film (such as a membrane protein or a surface adsorbed macromolecule) [39]. We show that for membranes under tension, stable protruding circular domains (we call these *caplets*, as in Refs. [32,35]) similar to those observed for mixtures of lecithin and phosphatitic acid [36] can occur at low concentrations of the minority component or impurity. We illustrate the structure of such circular *caplet* domains in Fig. 2. We also demonstrate the possibility of a phase transition from a mesophase of circular caplets to a mesophase of protruding stripe domains either with increasing area fraction of the minority component or with increasing tension. We illustrate these stripe domains in Fig. 2.

In both cases, the domains are shown to be stable with respect to complete phase separation in a flat membrane. In

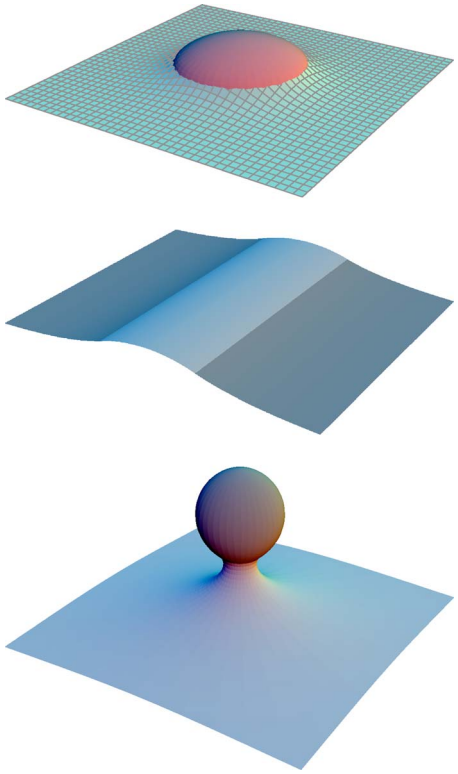

FIG. 2. (Color online) Schematic representation of phase-separated circular (top) and stripe (middle) domains and a bud (bottom) of the B component, with induced deformations.

Sec. II we present our model and briefly discuss our analysis in the Monge gauge treatment. In Sec. III, we provide the resulting Euler-Lagrange equations and boundary conditions used in our Monge gauge calculations. In Sec. IV we present Monge limit results in the dilute and concentrated regimes and discuss the extent to which the limiting approximations of Ref. [32] apply. In Sec. V we present the results of a numerical calculation of the budding transition beyond the Monge approximation, and we conclude in Sec. VI with a summary and discussion.

II. MODEL (MONGE GAUGE)

We consider a single idealized two-component membrane consisting of incompatible amphiphiles A and B. Furthermore, we consider asymmetric bilayers, in which phase separation occurs in only one leaflet of the bilayer, as shown in Fig. 1(b). This applies, for instance, to the case of phase separation in an asymmetric bilayer vesicle or biomembrane. Such domains can also be induced by the adsorption of macroions on the inside or outside of a bilayer vesicle, as in the experiments of Refs. [7,40]. We assume that the binary liquid mixture is far from its critical point, implying that there are sharp interfaces between the domains of A and B and that the membrane consists of a fluid minority phase B surrounded by an asymptotically flat fluid majority phase A.

We investigate the properties of two prototypical domain morphologies (see Fig. 3), which are idealizations of actual structures that may exhibit disordered textures of polydis-

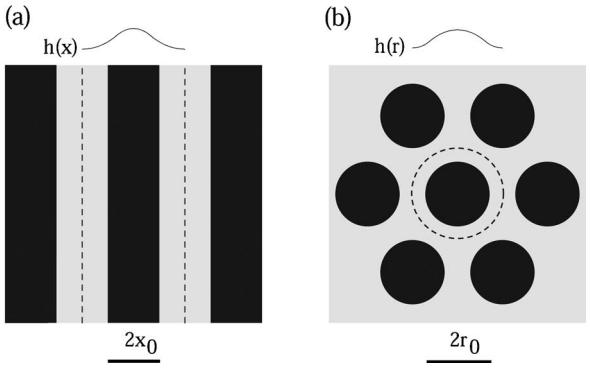

FIG. 3. A sketch of the stripe and caplet morphologies. (a) shows a linear array of B-phase stripes of width $2x_0$ (black) in a matrix of phase A (grey). (b) shows a hexagonal array of B-phase circular caplets of radius r_0 (black) in a matrix of phase A (grey). The dashed lines in each figure show the appropriate Wigner-Seitz cell boundaries, while the membrane displacement profile of an appropriate unit cell cross section is shown above each figure.

perse, irregular domains. These are the following:

(i) Quasi-one-dimensional domains of B (stripes), with an impurity phase of width $2x_0$ embedded inside a majority stripe with total with $2X_0$. The stripe length (system dimension) is L, and the projected area of an element (minority plus majority repeat unit) is $S_{A,\perp}+S_{B,\perp}=2X_0L$.

(ii) Monodisperse circular domains of B (caplets). For caplets we take a circular Wigner-Seitz cell with impurity radius r_0 and total radius R_0. The circular Wigner-Seitz cell approximation leads to a lower bound for the free energy of a less symmetric structure, such as a hexagonal array. The projected area of an element is $S_{A,\perp}+S_{B,\perp}=\pi R_0^2$.

Below we will typically scale these dimensions by the spontaneous curvature c_0, thus defining $\rho_0=r_0c_0$, $\bar{R}_0=R_0c_0$, $\xi_0=x_0c_0$, and $\Xi_0=X_0c_0$.

For given material parameters, we obtain minimum energy height profiles $h(\mathbf{r})$ (within a linearized Monge gauge description), where $\mathbf{r}$ is the position in the plane, and minimize the resulting free energy over the domain dimensions. We consider the background A phase to be flat and restrict our attention to the simplified case of equal bending moduli $\kappa_A=\kappa_B\equiv\kappa$.

For phase-separated membranes under tension, the free energy of a single domain (stripe or caplet) has the form

$$G_0 = F_l + F_s + F_b, \tag{2.1}$$

where F_l, F_s, and F_b are the energy contributions from the interfacial (line) tension between the two phases, the membrane frame (surface) tension, and the bending elasticity. To lowest order in the Monge representation (see Appendix A), valid for nearly flat membranes, these contributions relative to a flat reference state are given as follows.

The bending energy is

$$F_b = \frac{1}{2}\kappa\left\{\int_{S_A}(\nabla^2 h)^2 dS_\perp + \int_{S_B}[(\nabla^2 h)^2 - 2c_0\nabla^2 h + c_0^2(\nabla h)^2]dS_\perp\right\}, \tag{2.2}$$

where $dS_\perp$ is the (flat) area measure in the plane, S_i denotes the projected area occupied by phase i, $h(\mathbf{r})$ is the height profile above some flat reference plane, ∇ is a two-dimensional gradient operator, κ is the bending modulus, and c_0 is the spontaneous curvature of the B phase. The line tension energy is

$$F_l = \lambda\oint_{\partial S_B} dl = \begin{cases}\lambda 2\pi r_0 N & \text{(caplets)},\\ \lambda 2LN & \text{(stripes)},\end{cases} \tag{2.3}$$

where N is the number of domains, ∂S_B denotes the boundary of the impurity region, and λ is the line tension. The work done by the membrane in deforming relative to the flat state is

$$F_s = \frac{1}{2}\left\{\sigma\int_{S_A}|\nabla h|^2 dS_\perp + (\sigma+\mu)\int_{S_B}|\nabla h|^2 dS_\perp\right\}, \tag{2.4}$$

where σ is the frame tension and the Lagrange multiplier (or exchange chemical potential per unit area) μ controls the amount of impurity phase. We assume a fixed area per molecule in the membrane, and thus ignore stretching energies.

It will be convenient to define a renormalized chemical potential $\tilde{\mu}$, by

$$\tilde{\mu} = \mu + \kappa c_0^2, \tag{2.5}$$

where κc_0^2 arose in Eq. (2.5) from keeping all terms to second order in the height field [35]. This renormalization, neglected in [32], is typically very small: κc_0^2 is of order k_BT divided by a curvature radius squared of order $(100\ \text{nm})^2$, while $\sigma\sim k_BT$ divided by a length squared of order nm^2. In fact, we will find that this renormalization does not change the phase boundaries if only one phase has a nonzero spontaneous curvature; see [35] for a different example.

Stationarity of Eq. (2.1) with respect to height variations leads to Euler-Lagrange (EL) equations for the height profiles in regions A and B. The detailed derivation of the these equations is presented in Appendix A. To calculate the phase behavior we must minimize the free energy G of an array of domains,

$$G(\mu,\sigma,\lambda) = NG_0(\mu,\sigma,\lambda), \tag{2.6}$$

where

$$N = \frac{S_{fr}}{S_{A,\perp}+S_{B,\perp}} \tag{2.7}$$

is the number of domains and S_{fr} is the frame area, which without loss of generality we consider to be fixed. The free energy must also be minimized over the dimensions of the A and B domains, x_0 and X_0 for the stripes and r_0 and R_0 for the caplets:

$$\frac{\partial G}{\partial x_0} = 0, \quad \frac{\partial G}{\partial X_0} = 0 \quad \text{(stripes)}, \tag{2.8a}$$

$$\frac{\partial G}{\partial r_0} = 0, \quad \frac{\partial G}{\partial R_0} = 0 \quad \text{(caplets)}. \tag{2.8b}$$

Physically, minimization over the inner length (x_0 or r_0) is equivalent to allowing exchange of B for A species, while minimization over the outer length (X_0 or R_0) is equivalent to allowing more or less total area into the system, doing work against the frame tension.

Phase coexistence is found by equating chemical potentials,

$$\mu_{\text{stripes}} = \mu_{\text{caplets}}. \tag{2.9}$$

In the dilute limit, where all the impurity is in a single domain, we must minimize the free energy per impurity,

$$g(\mu, \sigma, \lambda) = \frac{G_0(\mu, \sigma, \lambda)}{S_{B,\perp}}, \tag{2.10}$$

over the impurity domain size. In using the projected area of the B phase we have kept terms consistent with the Monge gauge calculation (and hence ignored a term of order h^2 in the denominator).

Following [32], we will use *careted* variables for dimensionless quantities $\hat{\lambda}$, $\hat{\sigma}$, $\hat{\mu}$ (introduced below and Appendix A) scaled by κ and appropriate powers of c_0 and unadorned variables for physical quantities. This differs from the more recent work of [35] in which dimensional quantities were careted and dimensionless quantities were not careted.

For simplicity, we have also assumed that all bending moduli are the same in the different phases. Different mean curvature moduli κ will obviously shift the phase boundary in favor of the phase with a lower curvature modulus, while a difference in Gaussian curvature moduli would lead to a shape-dependent line tension that will shift the phase boundaries [33].

III. EULER-LAGRANGE EQUATIONS AND BOUNDARY CONDITIONS

Variation of $G_0(\mu, \sigma, \lambda)$ with respect to $h(\mathbf{r})$ gives the Euler-Lagrange equations for the height profile. To calculate the free energy we only need the slope $\eta = dh/dx$ (stripe) or $\eta = dh/dr$ (caplet). As shown in Appendix A, the slopes in regions A and B ($i = A, B$) satisfy

$$\frac{d^2\eta}{d\xi^2} - \zeta_i^{\,2}\eta = 0 \quad \text{(stripes)}, \tag{3.1a}$$

$$\frac{d^2\eta}{d\rho^2} + \frac{1}{\rho}\frac{d\eta}{d\rho} - \left(\zeta_i^{\,2} + \frac{1}{\rho^2}\right)\eta = 0 \quad \text{(caplets)}, \tag{3.1b}$$

where we have introduced the dimensionless variables,

$$\xi = c_0 x, \tag{3.2a}$$

$$\rho = c_0 r, \tag{3.2b}$$

$$\zeta_B^2 = \hat{\sigma} + \hat{\mu}, \tag{3.2c}$$

$$\zeta_A^2 = \hat{\sigma}, \tag{3.2d}$$

$$\hat{\sigma} = \frac{\sigma}{\kappa c_0^2}, \tag{3.2e}$$

$$\hat{\mu} = \frac{\tilde{\mu}}{\kappa c_0^2} + 1, \tag{3.2f}$$

$$\hat{\lambda} = \frac{\lambda}{\kappa c_0}. \tag{3.2g}$$

Note that the renormalization of μ due to κc_0^2 is identical in both stripe and caplet phases, and will thus play no role in determining coexistence—i.e., in Eq. (2.9).

Symmetry of η at the domain centers implies

$$\eta(0) = \eta''(0) = 0, \tag{3.3}$$

where primes denote derivatives with respect to either ρ or ξ. Another condition may be supplied by requiring a well-defined energy. A discontinuity in η would imply singular curvature at the boundary, leading to a nonphysical curvature energy in the region of the interface ∂_{S_B} between A and B phases. Hence we must have

$$[\eta_A - \eta_B]_{\partial_{S_B}} = 0. \tag{3.4}$$

The final boundary conditions follow from the variation of the height profile and are derived in Appendix A. In the dilute limit,

$$[c_B - c_A]_{\partial_{S_B}} = c_0 \quad \text{(torque)}, \tag{3.5}$$

$$\sigma\eta_A(\infty) - \kappa c_A'(\infty) = 0 \quad \text{(normal force)}, \tag{3.6}$$

$$c_A(\infty) = 0 \quad \text{(torque)}, \tag{3.7}$$

where $c(r)$ is the curvature:

$$c = \begin{cases} \eta' & \text{(stripes)}, \\ \dfrac{1}{\rho}\dfrac{\partial}{\partial\rho}(\rho\eta) & \text{(caplets)}. \end{cases} \tag{3.8}$$

Equations (3.5) and (3.7) are torque balances at the A-B interface [41] and at the system boundary, and Eq. (3.6) is the consequence of zero vertical force at the A-B interface. For the concentrated limit, the last two equations should be replaced by the equivalent result for periodic boundary conditions:

$$\eta_A|_{\partial_{S_B}} = c'|_{\partial_{S_B}} = 0 \quad \text{(concentrated regime)}. \tag{3.9}$$

IV. MONGE LIMIT: RESULTS

The general solutions to the Euler-Lagrange equations are given in Appendix B. Before discussing the phase behavior

in the general (concentrated) case, we discuss the dilute limit for large frame tensions, where several approximations simplify the results.

A. Dilute limit ($\hat{\sigma} \gg \hat{\mu} \simeq 0$)

Since the height profiles decay in the A phase with a characteristic length $\sqrt{\kappa/\sigma}$, the dilute limit is valid provided that the domains are separated by more than this length. The general solutions in the Monge gauge, Eqs. (B5) and (B16), have inverse penetration depths $\zeta_A = \sqrt{\hat{\sigma}}$ and $\zeta_B = \sqrt{\hat{\sigma} + \hat{\mu}}$. In the dilute limit and for large frame tension we may ignore $\hat{\mu}$ relative to $\hat{\sigma}$ in the penetration depths. Taking the limits $R_0 \to \infty$ and $X_0 \to \infty$, the solutions (given in Appendix B) reduce to

$$\frac{\eta(\xi)}{\eta_0} = \begin{cases} \dfrac{\sinh[\sqrt{\hat{\sigma}}\xi]}{\sinh[\sqrt{\hat{\sigma}}\xi_0]} & (\xi \leqslant \xi_0), \\ \exp[\sqrt{\hat{\sigma}}(\xi_0 - \xi)] & (\xi \geqslant \xi_0), \end{cases} \quad \text{(stripes)}, \tag{4.1}$$

and

$$\frac{\eta(\rho)}{\eta_0} = \begin{cases} \dfrac{I_1[\sqrt{\hat{\sigma}}\rho]}{I_1[\sqrt{\hat{\sigma}}\rho_0]} & (\rho \leqslant \rho_0), \\ \dfrac{K_1[\sqrt{\hat{\sigma}}\rho]}{K_1[\sqrt{\hat{\sigma}}\rho_0]} & (\rho \geqslant \rho_0), \end{cases} \quad \text{(caplets)}, \tag{4.2}$$

where

$$\eta_0 = \begin{cases} [\sqrt{\hat{\sigma}}(1 + \coth\sqrt{\hat{\sigma}}\xi_0)]^{-1} & \text{(stripes)}, \\ \rho_0 I_1[\sqrt{\hat{\sigma}}\rho_0] K_1[\sqrt{\hat{\sigma}}\rho_0] & \text{(caplets)}. \end{cases} \tag{4.3}$$

Substituting these profiles into Eq. (2.1), the free energy per impurity of a single domain is (recall that we set $\hat{\mu} = 0$ in the dilute limit)

$$\frac{G_0}{S_{B,\perp}} = \begin{cases} \dfrac{1}{\xi_0}\left[\hat{\lambda} - \dfrac{1}{2}\eta_0\right] & \text{(stripes)}, \\ \dfrac{1}{\rho_0}[2\hat{\lambda} - \eta_0] & \text{(caplets)}, \end{cases} \tag{4.4}$$

where the impurity area $S_{B,\perp}$ is $2Lx_0$ (stripes) or πr_0^2 (caplets). The free energies can be rewritten as

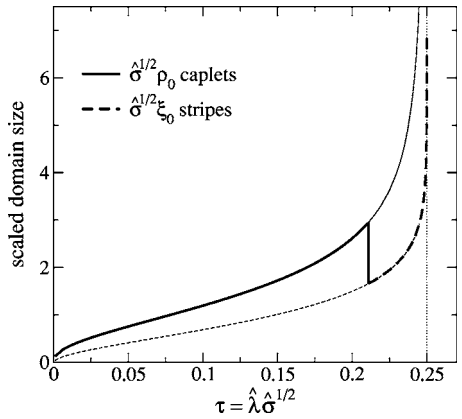

FIG. 4. Reduced domain size as a function of τ in the dilute limit ($\phi \to 0, \hat{\mu} \to 0$). The solid lines denote the stable phase. Caplets are stable for $\tau \lesssim 0.2115$, and stripes are stable for $0.2115 \lesssim \tau < 0.25$. For $\tau > 0.25$ the stable state is a macroscopically phase separated flat phase.

$$\frac{G_0}{S_{B,\perp}} = \begin{cases} \dfrac{\left[\tau - \dfrac{1}{2}(1 + \coth\sqrt{\hat{\sigma}}\xi_0)^{-2}\right]}{\sqrt{\hat{\sigma}}\xi_0} & \text{(stripes)}, \\ \dfrac{[2\tau - \sqrt{\hat{\sigma}}\rho_0 I_1(\sqrt{\hat{\sigma}}\rho_0) K_1(\sqrt{\hat{\sigma}}\rho_0)]}{\sqrt{\hat{\sigma}}\rho_0} & \text{(caplets)}, \end{cases} \tag{4.5}$$

so that the phase diagram in the dilute limit only depends on the control parameter $\tau \equiv \hat{\sigma}^{1/2}\hat{\lambda}$.[1] Minimizing the free energies over the periods yield the equilibrium domain sizes, shown in Fig. 4. The caplet phase is stable with respect to stripes for $\tau \lesssim 0.2115$, while stripes are unstable with respect to a flat phase for $\tau > 0.25$.

The stripe domain size diverges as the limit $\tau = 0.25$ is approached as

$$\lim_{\tau \to 0.25} \xi\hat{\sigma}^{1/2} = \frac{1}{2}\ln\left(\frac{2}{4\tau - 1}\right), \tag{4.6}$$

while the caplet radius grows from zero for small τ as

$$\lim_{\tau \to 0} \rho\hat{\sigma}^{1/2} = \left[\frac{4\tau}{3}\ln\left(\frac{1}{4\tau}\right)\right]^{1/3}. \tag{4.7}$$

Thus, the domain size diverges as either the line tension or the surface tension becomes large. The latter case simply corresponds to the fact that for large surface tensions there will be complete phase separation in a nearly flat two-dimensional system. The former case is somewhat more subtle, although, as we shall see, this limit corresponds to budding, since the resulting slope η_0 above becomes large.

B. Finite concentration of the B phase

For finite impurity concentration of the two phases, the the effective surface tensions of the two phases differ by the

[1] An analogous stability limit was derived for the model in Ref. [26] for stripes in the strong segregation limit.

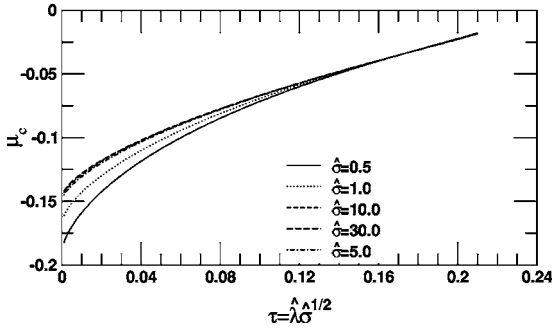

FIG. 5. Chemical potential as a function of generalized tension for different frame tensions $\hat{\sigma}$. Note the extrapolation to small $\hat{\mu}$ with increasing τ.

chemical potential (Lagrange multiplier) μ, which cannot strictly speaking be ignored. In this case the phase diagram does not depend solely on the dimensionless quantity $\tau = \hat{\lambda}\hat{\sigma}^{1/2}$. This was also noted by Góźdź and Gompper, in the case of systems with two different spontaneous curvatures [35]. However, we will see that the reduction to a phase diagram that depends only on τ is an excellent approximation in many cases.

For finite area fraction ϕ of the B phase, we assume a regular array of monodisperse (stable) domains, each within cell dimensions determined by the concentration. We approximate the hexagonal Wigner-Seitz cell (see Fig. 3) by a set of circular domains of equal area [42]. The solutions are given by Eqs. (B5) (stripes) and (B16) (caplets), with corresponding free energies $\hat{g}$ given by Eqs. (B10) and (B20). To calculate the phase diagram we minimize the free energies over both domain dimensions (x_0 and X_0 for stripes, r_0 and R_0 for caplets) for a given set of control parameters (line tension $\hat{\lambda}$, frame tension $\hat{\sigma}$, chemical potential $\hat{\mu}$) and determine the phase boundaries by that chemical potential $\hat{\mu}$ for which the free energies of the caplet and stripe phases are the same.

Our procedure differs slightly from that of Ref. [32] in that, here, the effective overall "tension" is different in the two phases. In the impurity phase B the quantity $\hat{\sigma}+\hat{\mu}$ acts like a mechanical tension penalizing area changes, while (because we have chosen a reference chemical potential $\hat{\mu}_A=0$) only $\hat{\sigma}$ penalizes area changes in the A phase. Hence the inverse penetration lengths ζ_A and ζ_B differ. In the strong tension limit $\hat{\sigma} \gg \hat{\mu}$, which is exact for vanishing ϕ where $\hat{\mu}$ becomes quite small (see Fig. 5), this approach recovers the results of Ref. [32], while for smaller $\hat{\sigma}$ the height profile of the impurity phase contains a contribution from the chemical potential as well as the frame tension. In the limit $\hat{\sigma} \gg \hat{\mu}$ where the penetration depths are the same, the phase diagram depends on only the generalized reduced tension τ.

With increasing ϕ, the domains grow monotonically with $r_0(\phi) \simeq 2\xi_0(\phi)$, which corresponds to nearly equal mean curvature $c \sim c_0$. Note that a finite preferred domain size implies the existence of an equilibrium mesophase. With increasing ϕ there is a first-order transition from circular caplets to stripes for small τ (Fig. 6). For small τ the transition depends very weakly on τ and coexistence occurs over a range of concentrations near $\phi=0.35$. This range moves to smaller

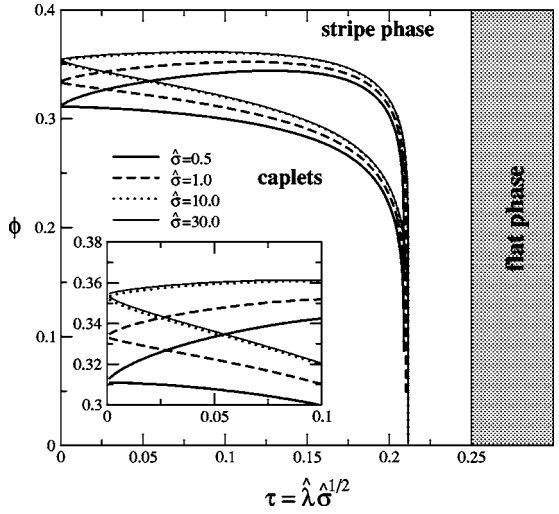

FIG. 6. Phase diagram as a function of B-phase area fraction ϕ and generalized reduced tension τ, for different constant frame tensions $\hat{\sigma}$ ($\hat{\lambda}$ was varied to scan τ). The region between upper and lower pairs of lines are two-phase regions of coexisting stripes and caplets. The inset shows convergence for large $\hat{\sigma}$ near the small τ phase boundary. An equilibrium flat phase is predicted for $\tau > 0.25$. Scans for different $\hat{\sigma}$ converge to the results of Ref. [32], which corresponds to the limit $\hat{\sigma} \to \infty$.

concentration with increasing τ, while for $0.2115 < \tau < 0.25$; however, the stripe phase becomes stable at all concentrations.

Figures 5–7 show that for large $\hat{\sigma}$ the phase diagrams converge to a scaling form that depends only on τ, recovering the phase diagram calculated in Ref. [32]. For larger $\hat{\sigma}$ the concentration range of the stable caplet phase widens at small τ, moving to larger ϕ. Recall, Eq. (3.2c), that the characteristic inverse decay length in the impurity phase is $\zeta_B = \sqrt{\hat{\sigma}+\hat{\mu}}$, where we find $\hat{\mu} < 0$ along the phase boundary. Hence, for a smaller tension $\hat{\sigma}$ the negative potential decreases the energetic cost of buckling against tension, which destabilizes the stripe phase. The deviation of the phase

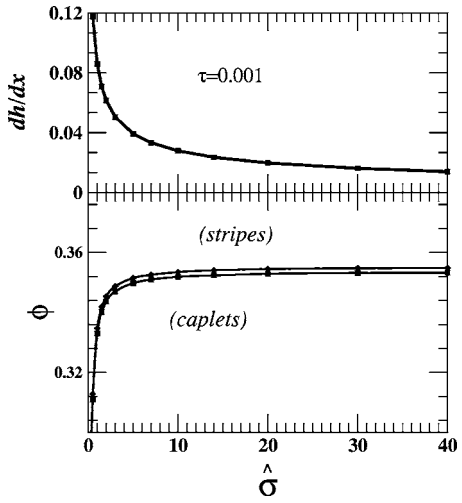

FIG. 7. Phase boundaries ϕ_{caplet} and ϕ_{stripe} and stripe and caplet slopes dh/dx for fixed $\tau=0.001$ and varying $\hat{\sigma}$.

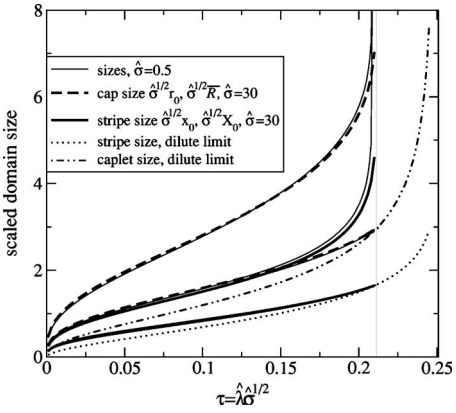

FIG. 8. Scaled domain sizes for caplet and stripe phases along the phase coexistence line, for both the concentrated and dilute limit calculations. For each geometry the two dimensions (stripe half-period ξ_0 and minority domain half width Ξ_0, and caplet inner radius ρ_0, and Wigner-Seitz radius $\bar{R}$, all scaled by $\hat{\sigma}$) are shown. The variation in domain sizes with tension $\hat{\sigma}$ can be seen to be very small.

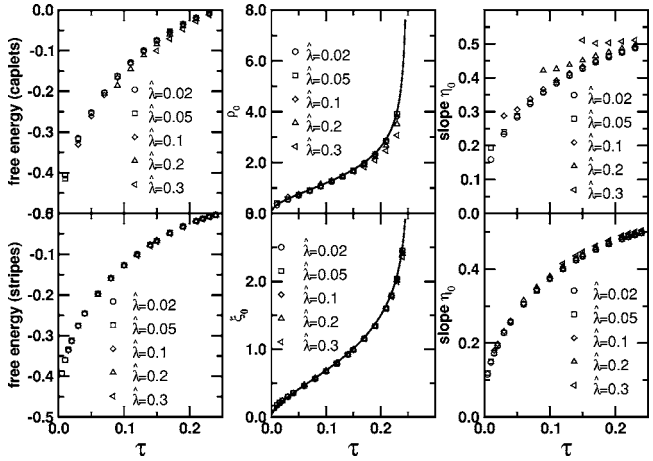

FIG. 9. Data collapse of the free energy per unit area (in units of κc_0^2), domain size (units of c_0), and boundary slope as a function of τ for both stripes and caplets, for various values of the line tension $\hat{\lambda}$.

boundary near $\tau \simeq 0.2115$ is due to departures from the Monge limit.

The length scales in the concentrated limit are larger than in the dilute limit, for the same τ, and converge to the dilute limit result when the caplet phase loses stability at $\tau \simeq 0.2115$, as expected (Fig. 8).

V. NUMERICAL SOLUTIONS IN THE BUDDING REGIME

The calculations presented above and in Ref. [32] are based on a small-slope approximation and are only valid for small line tension λ or large frame tension σ. In order to both test the validity of this approximation as well as to study the possible transition from the caplet state above to a budded states, we have performed direct numerical minimization of the model free energy in Eq. (2.1), beyond the small-slope approximation. We present here the equilibrium shapes and phase diagram for the stripe phase, the (azimuthally symmetric) caplet phase and for buds.

We focus on the dilute limit—i.e., for small area fraction ϕ. It is expected that phase separation may, under appropriate conditions, lead to the formation of buds (nearly spherical domains of one phase connected with a narrow neck to another phase that is flat). It has previously been shown theoretically that the line tension between two phases alone may result in budding [28,43]. The role of phase separation in budding and fission has also been studied in recent experiments [44]. As described above, our small-slope approximation used in the previous sections is expected to fail for large line tension λ.

In order to address both the validity of the preceding analysis, as well as to treat possible budding transitions, we describe the membrane shape by a local tangent angle θ relative to a horizontal, flat conformation. For a stripe domain, the shape can be completely characterized by the tangent angle as a function of only one contour length coordinate s, which is defined along a line perpendicular to the stripe. For a caplet or bud domain, a single tangent angle as a function of a single coordinate s can also be used to completely describe the membrane shape, even in the presence of overhangs. This can be done provided that the domain is symmetric about an axis perpendicular to a horizontal plane. In this case, the contour length coordinate is defined along a radial direction. A similar approach was used in [35].

If the center of the domain is taken as the origin, then the membrane shape in three dimensions is given by

$$(x(s),y(s),z(s)) = (r(s)\cos(\phi),r(s)\sin(\phi),z(s)), \quad (5.1)$$

where $r(s)=\int\cos(\theta)ds$ is a radial coordinate, $z(s)=\int\sin(\theta)ds$, and ϕ is the azimuthal angle. In this coordinate system, the mean curvature is given by

$$H = \frac{d\theta}{ds} + \frac{\sin\theta}{r} \quad (5.2)$$

for caplet and bud domains. For stripes, only the first term above is necessary.

The resulting free energy is evaluated numerically for a domain shape defined by a discrete set of 50–200 angles $\{\theta_i\}_{i=0,\ldots,N}$, which are defined at equally spaced points s_i along the contour from the origin to the Wigner-Seitz boundary described previously. These values, together with an overall scale factor $\Delta s = s_{i+1} - s_i$, determine the membrane shape.

A discrete approximation to the free energy f per unit area of domain is minimized to determine equilibrium shape and free energy. Here, we quote results for an area fraction of 10%. As shown above within the small-slope approximation, the phase boundary between stripes and caplets is very narrow and relatively insensitive to area fraction in this range. In Fig. 9, we show the normalized stripe domain size (ξ_0), boundary slope (η_0), and free energy f vs τ for several different combinations of $\hat{\sigma}$ and $\hat{\lambda}$. The apparent collapse of the data demonstrates one of the conclusions of the previous analysis: namely, that the results can be well represented in

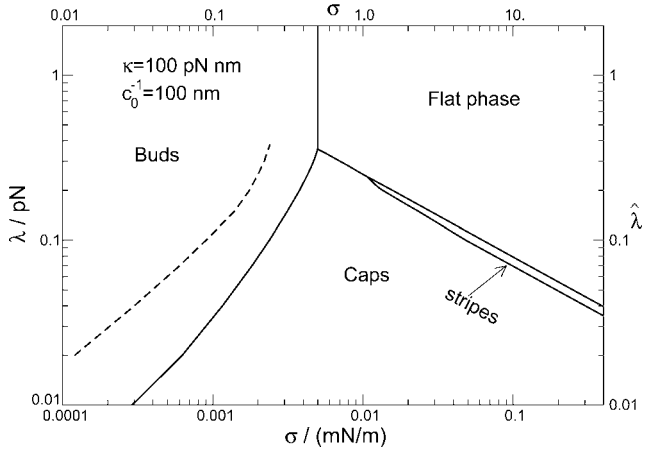

FIG. 10. The calculated phase diagram, indicating bud, caplet, and stripe phases, as well as the flat phase corresponding to macroscopic phase separation. This has been obtained by the numerical procedure outlined in Sec. V. The solid lines indicate thermodynamic phase boundaries, while the dashed line indicates the limit of metastability of caplets. As discussed in the text, we expect that buds are metastable throughout the phase diagram, within the approximations used here. The thin region shown is that of the stripe phase. This vanishes at a triple point near $(\hat{\sigma},\hat{\lambda})=(1.0,0.25)$. The bud, caplet, and flat phases meet at the other triple point along $\hat{\sigma}=0.5$. Upper and right-hand axes are dimensionless, while lower and left-hand axes are in physical units for typical values of the bending energy and spontaneous curvature, $\kappa=100$ pN nm, $c_0^{-1}=100$ nm.

terms of a single combination of parameters, $\tau=\hat{\lambda}\sqrt{\hat{\sigma}}$, of surface tension and line tension. Similar results for caplet domains are shown in Fig. 9. Here, too, the results show the dependence on the single parameter τ.

These numerical results can also be used to determine the phase boundary between the caplet and stripe phases. For simplicity, we do this only in the dilute limit, in which the phase boundary is rather insensitive to concentration. Specifically, we find the crossing of the free energies of the caplet and stripe phases (f_c and f_s) for 10% area fraction. The results are shown in Fig. 10. We note the excellent agreement of this phase boundary with that shown in Fig. 6, at least for $\hat{\lambda}\lesssim 0.2$. For larger $\hat{\lambda}$ the former approximations fail. One consequence of this is that the stripe phase vanishes with increasing $\hat{\lambda}$: specifically, there is a narrow range of values of the line tension for which the only stable domains are caplets. This can be seen in Fig. 10. The simple physical reason for the enhanced stability of the caplet phase (compared with the small-slope results above) in this limit is that the line tension cost is lowered in the caplet geometry for large slopes, given a fixed domain area: for caplets, the circumference to area ratio is reduced with increasing slope.

Also shown in Fig. 10 is the transition between caplet and bud states, as well as a spinodal line beyond which no stable caplet structures are possible. No spinodal representing the limit of metastability of buds is found. This is an artifact of the use of a bending free energy using only leading order terms. Such a spinodal depends on the details, and especially the radius a of the neck in the budded state. Without further assumptions, this length shrinks to of order Δs. The surface tension required to pull out such a bud is of the order of the two-dimensional Laplace "pressure" $\sigma\sim\lambda/a$, which diverges for small necks. Thus, this spinodal cannot be reliably determined, if at all, by our numerical scheme. Within the approximation that the neck of the budded state shrinks to a size much smaller than the domain size, we find that buds are, in fact, metastable throughout the phase diagram. This is because, for small necks, there is a linear increase in the free energy due to the line tension when the neck expands, while both bending and surface tension contributions are quadratic.

The remaining phase boundary shown in Fig. 10 is that of the transition from the flat phase (macro phase separation) to the budded state. This phase boundary is simple to estimate. The free energy per unit area of the bud is simply $-\frac{1}{2}\kappa c_0^2$, while the bud accounts for an excess area of $4\pi(2/c_0)^2$, assuming an optimal mean curvature of c_0. As noted above, the radius of the neck tends to zero. This results in a phase boundary given by $\hat{\sigma}=1/2$ in reduced units. This simple phase boundary estimate is well borne out by the numerical minimization, as shown in the figure.

VI. DISCUSSION

The transition from caplets to stripes that occurs at small $\hat{\mu}$ with increasing ϕ and τ can be understood in simple physical terms. The unit cell ϕ the unit cells in the stripe and caplet morphologies scale as $X_0\sim 1/\phi$ and $R_0\sim 1/\sqrt{\phi}$, respectively. With increasing ϕ, the constraints on the membrane profiles due to the shrinking unit cell boundaries become more costly in the caplet phase than the stripe phase, thereby favoring the stripe phase at large ϕ. Alternatively, with increasing generalized tension τ, the regions of largest slope (and therefore largest difference between projected area and membrane area) near the domain boundaries become energetically more costly because of the work required against tension. For caplets, this represents a larger fraction of the domain area than for stripes. Thus, stripes are preferred for sufficiently large τ in the limit of small line tension.

From the numerical approach of the previous section, we see, perhaps surprisingly, that the Monge approximation works rather well to describe the various phases and transitions. Specifically, we see from Fig. 9 that for $\hat{\lambda}\lesssim 0.2$ there is little disagreement between the Monge approximation and the numerical solutions that can account for finite slopes. This is particularly true of the caplet phase.

In general, we expect the Monge approximation to be best for large $\hat{\sigma}$, which tends to flatten the membrane. Since the phase boundaries between caplets, stripes, and the flat phase tend to occur for a fixed $\tau=\hat{\sigma}^{1/2}\hat{\lambda}$ (specifically $\tau\simeq 0.21$ and $\tau=0.25$ for the caplet-stripe and stripe-flat boundaries, respectively, in the dilute limit), we expect the Monge approximation to be valid near both transitions, except for large λ, which is what we find. Here, of course, σ tends to be smaller.

As noted above, however, the discrepancy is smaller for the caplet phase. The deviation that we find for stripes sug-

gests an instability toward larger domains and, ultimately, the flat phase. This tends to be compensated in the case of caplets by the line tension λ, which prevents domains from growing. This enhanced stability of caplets is also consistent with the observation from the phase diagram in Fig. 10 that the caplet-stripe phase boundary shifts in favor of caplets as λ increases. We find, in fact, a triple point, where caplet, stripe and flat phases meet, although this is hard to see in the figure. For larger λ, no stripe phase is observed.

Away from these transitions, however, we begin to see significant deviation from the Monge results for the largest λ as sigma decreases. Thus, the Monge approximation tends to fail to the left in Fig. 10. In particular, the Monge approximation is insufficient to characterize the transition between buds and caplets.

Our work shares some common features with previous theoretical studies. Undulating stripe and hexagonal phases in weakly segregated two-component membranes were first studied theoretically using a phenomenological coupling of local membrane composition and shape [22]. These phases are analogous to the strongly segregated stripe and caplet phases discussed in this paper. Moreover, the approach of Ref. [22] has recently been utilized to study one-dimensional shape profiles of two-component membranes and vesicles in the strong segregation regime [25,26]. The stripe phases of planar membranes in the limit of small domains or large bending energies presented in Ref. [26] are qualitatively similar to our stripe mesophases. The equilibrium stripe and cap membrane phases reported here should occur in phase-separated two-component films under tension, provided that one phase has finite spontaneous curvature and that the line and surface tensions are sufficiently small. While the calculations presented above assumed an asymptotically flat matrix phase, as in the case of a globally flat monlayer or bilayer membrane, our results should also be qualitatively valid for spherical bilayer vesicles, provided that the vesicle diameter D is sufficiently large compared with the characteristic domain dimension, i.e., if $c_0 D \gg 1$.

Góźdź and Gompper performed a similar calculation to ours in a different "slice" of parameter space. They considered phases with *different* signs of spontaneous curvature and predicted a variety of different budding, stripe, and circular domains. It is difficult to compare the results directly, since they chose only one parameter set $\hat{\lambda}=0.5$, $\hat{\sigma}=0.4$. For our model, with just one spontaneous curvature, this leads to a budded state. They show that this set of parameters can lead to a variety of phases that can be stabilized by the different spontaneous curvatures.

We estimate the region of domain stability for the following values of the parameters in our model:

$$\kappa = 25 k_B T \simeq 100 \text{ pN nm}, \quad c_0^{-1} = 100 \text{ nm}. \qquad (6.1)$$

The results are shown schematically in Fig. 10. Thus, caplet domains of order 100 nm in size (as in Ref. [40]) are stable for line tensions $\lambda \lesssim 0.3$ pN and surface tensions $\sigma \sim 10^{-2}$ mN/m. For comparison, membrane rupture occurs for surface tensions of order 10 mN/m [3].

Finally, we wish to note a couple of important general observations relevant to phase separating membrane systems. First, given the coupling between membrane composition and shape, it is possible to have both composition-induced changes in shape or curvature [21,29,31], as well as curvature-induced changes in composition [30]. However, unless the curvature is of a molecular scale (i.e., if curvature radii are comparable to the size a of a single lipid), it is generally expected that composition will drive shape, or, in other words, that chemistry determines geometry. This is because, on a per molecule basis, the curvature energy $\kappa a^2 c_0^2$ is very small compared with kT. Thus, unless one happens to be very close to a critical point [30], the shift in chemical potential due to the local curvature of the membrane is expected to be insufficient to cause a significant composition change. Second, the Gaussian curvature and associated modulus $\bar{\kappa}$, which we have so far neglected, is expected to affect the stability of the caplet and budded phases described above. In fact, this can have an order one effect on both phases, since the corresponding shift on the curvature energy is of order $\Delta\bar{\kappa} c_0^2$ per unit area, where $\Delta\bar{\kappa}$ represents the difference in moduli between the two phases. This is comparable to the (mean) curvature energy contribution in both phases. There will be no effect, however, on the stripe phase free energy. Thus, the main qualitative effect of taking into account the Gaussian curvature effects will be on the stability of the bud and caplet phases relative to the stripe phase. For instance, the expected increase or decrease in the energy of bud and caplet phases may result in a more pronounced or even absent stripe. Finally, we have imposed the strong segregation limit, in which the compositions of the two phases are unaffected by the local bending. This is likely to break down near critical points, at which point the compositions will vary in concert with the degree of bending [22–27]. In this case the local line tension can be expected to be lower and depend on the degree of local membrane deformation. Moreover, elastic constants and the spontaneous curvature will be inhomogeneous in the more highly deformed regions. Possible effects of this could be to stabilize the caplet phase in favor of the stripe phase (since line tension may be reduced), as well as shifting other phase boundaries. However, as we have emphasized above, the strong segregation limit is expected to apply more generally, because of the wide separation of scales between the molecular and curvature lengths.

ACKNOWLEDGMENTS

We thank A. Ajdari, F. Jülicher, D. Morse, J. Prost, R. Ross, and E. Sackmann for useful discussions and comments. F.C.M. acknowledges support from the NSF (Grant No. DMR-9257544), the Donors of the Petroleum Research Fund, and the Exxon Education Foundation. P.D.O. and F.C.M. acknowledge NATO Grant No. CRG 960678. All three authors thank the (K)ITP UCSB and the Isaac Newton Institute for Mathematical Sciences, where portions of this work were also performed. The authors wish to thank the ICTPC for a stimulating environment.

APPENDIX A: DERIVATION OF FREE ENERGY IN MONGE GAUGE

In this appendix we derive the free energy and boundary conditions for the Monge gauge calculation.

1. Free energy variation

Consider an impurity phase arranged into domains. The free energy is given by Eq. (2.1). The bending free energy with respect to a flat reference state is given by

$$F_b = \frac{1}{2}\kappa \int_{S_B} dS[c(r)^2 - 2c(r)c_0 + c_0^2] + \frac{1}{2}\kappa \int_{S_A} dS c(r)^2, \tag{A1}$$

where $c(r)$ is the mean curvature, c_0 is the spontaneous curvature of the impurity phase, κ is the bending modulus, and dS is the surface area. The structure has a frame tension σ against which the membrane does work, with energy

$$F_s = \sigma \left\{ A_{fr} - \int_{S_A+S_B} dS_\perp \right\}, \tag{A2}$$

where $dS_\perp$ is the projected membrane area and A_{fr} is the frame area. The line tension energy is proportional to the interface between phases A and B and is given by Eq. (2.3).

The membrane composition ϕ is given by

$$\phi = \frac{S_B}{S_B + S_A}. \tag{A3}$$

The two areas S_A and S_B are determined by the frame tension and a Lagrange multiplier μ to control the impurity phase B. Since we assume a constant area per lipid, μ is proportional to the chemical potential for B or, more strictly, the exchange chemical potential difference between A and B. We must minimize

$$G_0(\mu, \sigma, \lambda) = F_b + F_s + F_l + \mu \int_{S_B} dS \tag{A4}$$

over variations in the surface shape, $h(r) \to h(r) + \delta h(r)$, where the line tension energy F_l is given by Eq. (2.3). We will later minimize the resulting free energy over the domain dimensions.

In the Monge gauge in the two-dimensional geometry of the caplet case,

$$c(r) = \nabla^2 h = \frac{1}{\mathrm{r}} \frac{\partial}{\partial r}\left(r \frac{\partial h}{\partial r} \right), \tag{A5a}$$

$$dS = \left[1 + \frac{1}{2}(\nabla h)^2 \right]^{1/2} d^2 r, \tag{A5b}$$

$$dS_\perp = d^2 r, \tag{A5c}$$

and the variation of G over h leads, to lowest order in h,

$$\frac{\delta G}{2\pi} = \delta h(r_0) f_{hr}(r_0) + \delta h(R) f_{hR}(R) + \delta h'(r_0)\Gamma_r(r_0) + \delta h'(R)\Gamma_R(R) + \int_0^{r_0} d^2 r \, \delta h f_{e-l}^{\mathrm{B}} + \int_0^{R} d^2 r \, \delta h f_{e-l}^{\mathrm{A}}, \tag{A6}$$

in terms of the following forces f and torques Γ:

$$f_{hr} = 2\pi r[\kappa(c_A' - c_B') - (\sigma + \tilde{\mu})h_B' + \sigma h_A'], \tag{A7a}$$

$$f_{hR} = 2\pi R[\sigma h_A' - \kappa c_A'], \tag{A7b}$$

$$\Gamma_r = 2\pi\kappa r(c_B - c_A - c_0), \tag{A7c}$$

$$\Gamma_R = 2\pi R \kappa c_A. \tag{A7d}$$

Here we have defined $\tilde{\mu} = \mu + \kappa c_0^2$, which is consistent with a complete expansion to second order in h [35]. The Euler-Lagrange equations, which determine the profile $h(r)$, are

$$f_{e-l}^{\mathrm{B}} = \kappa(c_B' + r c_B'') - (\sigma + \tilde{\mu}) r c_B = 0, \tag{A8a}$$

$$f_{e-l}^{\mathrm{A}} = \kappa(c_A' + r c_A'') - \sigma r c_A = 0. \tag{A8b}$$

Because the free energy and the forces and torques depend only on derivatives of h, we will solve for the slope $\eta = dh/dr$ instead of the height profile.

Equations (A7) and (A8) are specific for the cylindrical geometry of the caplet morphology. The analogous set of equations for the stripe morphology is

$$\frac{f_{hr}}{L} = \kappa(c_A' - c_B') - (\sigma + \tilde{\mu})h_B' + \sigma h_A', \tag{A9a}$$

$$\frac{f_{hR}}{L} = \sigma h_\alpha' - \kappa c_A', \tag{A9b}$$

$$\frac{\Gamma_r}{L} = \kappa(c_B - c_A - c_0), \tag{A9c}$$

$$\frac{\Gamma_R}{L} = \kappa c_A, \tag{A9d}$$

$$f_{e-l}^{\mathrm{B}} = \kappa c_B'' - (\sigma + \tilde{\mu}) c_B = 0, \tag{A9e}$$

$$f_{e-l}^{\mathrm{A}} = \kappa c_A'' - \sigma c_A = 0, \tag{A9f}$$

where now h is a function of the Cartesian coordinate x and the curvature is given by $c = d^2h/dx^2$.

2. Boundary conditions

The boundary conditions are specified by the forces and torques applied to the membrane. There is no applied torque at the interface, r_0, and we assume no applied torque at the boundary,[2] so

$$\Gamma_r(r_0) = 0, \tag{A10a}$$

$$\Gamma_R(R) = 0. \tag{A10b}$$

In this appendix we will explicitly describe the boundary conditions for the two-dimensional caplet geometry; the same conditions hold for the one-dimensional stripe geom-

[2] Alternatively, we could specify the slope at the boundary R.

etry, with $r \to x_0$, unless noted. The second condition specifies zero curvature on the boundary while the first, first given by Kozlov and Helfrich, relates the difference in the mean curvature to the spontaneous curvature of the inner surface. Next, we assume there are no vertical forces applied to the membrane,

$$f_{hr}(r_0) = 0, \tag{A11a}$$

$$f_{hR}(R_0) = 0. \tag{A11b}$$

However, it is straightforward to show (for both the one- and two-dimensional cases) that these vertical boundary conditions are in fact proportional to first integrals of the Euler-Lagrange equations. Specifically, in two dimensions,

$$f_h(r) = r[\kappa c'(r) - \sigma h'(r)] \tag{A12a}$$

$$= \int dr f_{e-l}[h(r)] \tag{A12b}$$

$$= \text{const}. \tag{A12c}$$

Since $f_h(r)$ is constant for all r, the boundary condition at the junction, Eq. (A11a), is irrelevant and we are left with Eq. (A11b). A similar result applies for the one-dimensional stripe geometry.

To completely specify the problem we need a few more conditions. Symmetry about the domain center requires

$$h'_B(0) = h'''(0) = 0. \tag{A13}$$

Another condition on the derivative of the profile $h'(r_0)$ results by requiring a well-defined energy. If h' has a discontinuity at the boundary, then the curvature has a δ function as the boundary is crossed. This leads to a nonphysical and singular energy in the region of the junction $r=r_0$. Hence we are led to our final boundary condition

$$h'_B(r_0) = h'_A(r_0). \tag{A14}$$

For completeness, we reproduce the relevant boundary conditions that remain after recognizing the redundance of Eq. (A11a). For the single-domain problem, from Eqs. (A7b)–(A7d) we have

$$[c_B - c_A]_{r_0} = c_0, \tag{A15a}$$

$$\tau h'_A(\infty) - \kappa c'_A(\infty) = 0, \tag{A15b}$$

$$c_A(\infty) = 0. \tag{A15c}$$

The three equations above, together with the three conditions of Eqs. (A13) and (A14), give us six conditions. The Euler-Lagrange equations [Eqs. (A8)] are second-order differential equations for $c_B(r)$ and $c_A(r)$, which have four constants. The solutions to these equations must be integrated once to obtain $\eta(r)$, which yields six constants. Finally, we determine the domain size r_0 by minimizing the total free energy (after substituting the solution into the original free energy) over r_0. Hence we have a closed set of equations which determine the height profiles $h_B(r)$ and $h_A(r)$ and the impurity domain size r_0, for a given (arbitrary) frame area.

For the multidomain problem the boundary conditions must be modified. We still have Eqs. (A13) and (A14) above, but instead of boundary conditions at $R=\infty$, we impose a symmetric profile at the Wigner-Seitz cell boundaries:

$$c'_A(R) = h'_A(R) = 0, \tag{A16}$$

replacing Eqs. (A15b) and (A15c).

APPENDIX B: SOLUTIONS

1. Stripes

For stripe domains the Wigner-Seitz cell is an impurity stripe of width $2x_0$ embedded inside a majority stripe with total with $2X_0$. The curvature is $c=d^2\eta/dx^2$, and the Euler-Lagrange equations (A9) are

$$\kappa \frac{d^4 h_A}{dx^4} - \sigma \frac{d^2 h_A}{dx^2} = 0, \tag{B1a}$$

$$\kappa \frac{d^4 h_B}{dx^4} - (\sigma + \tilde{\mu}) \frac{d^2 h_B}{dx^2} = 0. \tag{B1b}$$

To calculate the free energy we only need the slope

$$\eta = \frac{dh}{dx}. \tag{B2}$$

Equations (B1) may be integrated once, with integration constant zero (all odd derivatives $d^{(n)}h/dx^n$ vanish at the origin). This leaves the following Euler-Lagrange equations:

$$\frac{d^2 \eta_A}{d\xi^2} - \hat{\sigma} \eta_A = 0, \tag{B3a}$$

$$\frac{d^2 \eta_B}{d\xi^2} - (\hat{\sigma} + \hat{\mu}) \eta_B = 0, \tag{B3b}$$

where we have introduced the dimensionless variables

$$\xi = x c_0, \tag{B4a}$$

$$\hat{\sigma} = \frac{\sigma}{\kappa c_0^2}, \tag{B4b}$$

$$\hat{\mu} = \frac{\tilde{\mu}}{\kappa c_0^2,} \tag{B4c}$$

$$\Xi = X_0 c_0. \tag{B4d}$$

Note that $\tilde{\mu}$ and σ both have dimensions of energy/area, because we have implicitly assumed an incompressible membrane with an unchanging area per molecule. The solutions are

$$\eta_B = \eta_0 \frac{\sinh \zeta_B \xi}{\sinh \zeta_B \xi_0}, \tag{B5a}$$

$$\eta_A = -\eta_0 \frac{\sinh \zeta_A(\Xi - \xi)}{\sinh \zeta_A(\Xi - \xi_0)}, \tag{B5b}$$

where

$$\eta_0 = [\zeta_B \coth \zeta_B \xi_0 + \zeta_A \coth \zeta_A(\Xi - \xi_0)]^{-1}, \tag{B6}$$

$$\zeta_B^2 = \hat{\sigma} + \hat{\mu}, \tag{B7}$$

$$\zeta_A^2 = \hat{\sigma}. \tag{B8}$$

The hyperbolic functions satisfy the conditions of zero slope at the domain center $\xi=0$ and domain boundary $\xi=\Xi$ [Eqs. (A13) and (A16)], while the amplitude η_0 is determined by the discontinuity of curvatures at $\xi=\xi_0$, according to Eq. (A15a).

After some rearrangement, the free energy [Eq. (A4)] may be written as

$$\frac{G_0}{2L\kappa c_0} = \lambda + \mu\xi_0 - \frac{\eta_0}{2}. \tag{B9}$$

The number of stripes is given by $N=A_{fr}/2\Xi L$ and the total free energy is $G=NG_0$. We can thus write the free energy per frame area $\hat{g}$, in dimensionless form, as

$$\hat{g} \equiv \frac{G}{\kappa c_0^2 A_{fr}} = \frac{1}{\Xi}\left[\lambda + \mu\xi_0 - \frac{\eta_0}{2}\right]. \tag{B10}$$

2. Caplets

We consider circular domains of inner radius r_0 and outer radius R. The Euler-Lagrange equations for the circular geometry, Eqs. (A8), are given by

$$\kappa(c_A' + rc_A'') - \sigma r c_A = 0, \tag{B11}$$

and similarly for c_B. In cylindrical coordinates, the mean curvature is

$$c(r) = \frac{1}{r}\frac{\partial}{\partial r}\left(r\frac{\partial h}{\partial r}\right). \tag{B12}$$

Equation (B11) may be integrated once to give

$$r\{\kappa c' - \sigma h'\} = \text{const}. \tag{B13}$$

Again, $h'(0)=c'(0)=0$ by symmetry, so the constant vanishes. As with the stripe case, we only need the slope

$$\eta = \frac{\partial h}{\partial r}, \tag{B14}$$

in terms of which Eqs. (A8) become

$$\frac{\partial^2 \eta_i}{\partial \rho^2} + \frac{1}{\rho}\frac{\partial \eta_i}{\partial \rho} - \eta_i\left(\zeta_i^2 + \frac{1}{\rho^2}\right) = 0 \tag{B15}$$

for $i=$A,B, where $\rho=rc_0$. Implementing the boundary conditions yields the following profiles:

$$\frac{\eta_B}{\eta_0} = \frac{I_1(\zeta_B\rho)}{I_1(\zeta_B\rho_0)}, \tag{B16a}$$

$$\frac{\eta_A}{\eta_0} = \frac{K_1(\zeta_A\rho) - AI_1(\zeta_A\rho)}{K_1(\zeta_A\rho_0) - AI_1(\zeta_A\rho_0)}, \tag{B16b}$$

with

$$A = \frac{K_1(\zeta_A\bar{R})}{I_1(\zeta_A\bar{R})}, \tag{B17}$$

$$\eta_0 = \frac{I_1(\zeta_B\rho_0)}{\zeta_A I_1(\zeta_B\rho_0)\dfrac{K_0(\zeta_A\rho_0) + AI_0(\zeta_A\rho_0)}{K_1(\zeta_A\rho_0) - AI_1(\zeta_A\rho_0)} + \zeta_B I_0(\zeta_B\rho_0)}, \tag{B18}$$

where $\bar{R}=Rc_0$ and I_0, I_1, K_0, and K_1 are modified Bessel functions [45]. The free energy per caplet is given by

$$\frac{G_0}{2\pi\kappa} = \lambda\rho_0 + \frac{1}{2}\rho_0(\rho\mu - \eta_0). \tag{B19}$$

The number of caplets is $N=A_{fr}/(\pi\bar{R}^2)$, so the total free energy per frame area is

$$\hat{g} = \frac{G}{\kappa c_0^2 A_{fr}} = \frac{\rho_0}{\bar{R}^2}[2\lambda + \rho_0\mu - \eta_0]. \tag{B20}$$

Equations (B20) and (B10) are used in Eqs. (2.8) to evaluate the equilibrium domain sizes [45].

[1] *Physics of Amphiphilic Layers*, edited by D. Langevin, J. Meunier, and N. Boccara (Springer, Berlin, 1987).
[2] G. Cevc and D. Marsh, *Phospholipid Bilayers* (Wiley, New York, 1987).
[3] R. B. Gennis, *Biomembranes* (Springer, Berlin, 1989).
[4] *Handbook of Biological Physics*, edited by R. Lipowsky and E. Sackmann (Elsevier, Amsterdam, 1995), Vol. 1.
[5] E. Farge and P. F. Devaux, Biophys. J. **61**, 347 (1992).
[6] H. G. Döbereiner, J. Käs, D. Noppl, I. Sprenger, and E. Sackmann, Biophys. J. **65**, 1396 (1993).
[7] E. Sackmann and T. Feder, Mol. Membr Biol. **12**, 21 (1995).
[8] A. Radhakrishnan and H. M. McConnell, Biophys. J. **77**, 1507 (1999).
[9] C. Rauch and E. Farge, Biophys. J. **78**, 3036 (2000).
[10] C. Leidy, W. F. Wolkers, K. Jorgensen, O. G. Mouritsen, and J. H. Crowe, Biophys. J. **80**, 1891 (2001).
[11] T. Baumgart, S. T. Hess, and W. W. Webb, Nature (London) **425**, 821 (2003).
[12] S. L. Veatch and S. L. Keller, Biophys. J. **85**, 3074 (2003).
[13] S. L. Veatch and S. L. Keller, Phys. Rev. Lett. **89**, 268101 (2002).
[14] S. L. Veatch, I. V. Polozov, K. Gawrisch, and S. L. Keller,

Biophys. J. **86**, 2910 (2004).
[15] S. Munro, Cell **115**, 377 (2003).
[16] M. Edidin, Annu. Rev. Biophys. Biomol. Struct. **32**, 257 (2003).
[17] K. Gaus, E. Gratton, E. P. W. Kable, A. S. Jones, I. Gelissen, L. Kritharides, and W. Jessup, Proc. Natl. Acad. Sci. U.S.A. **100**, 15554 (2003).
[18] D. D. Lasic, *Liposomes in Gene Delivery* (CRC Press, Boca Raton, FL, 1997).
[19] in *Medical Applications Of Liposomes* edited by D. D. Lasic and D. Papahadjopoulos (Elsevier, Amsterdam, 1998).
[20] J. N. Israelachvili, *Intermolecular and Surface Forces* (Academic Press, London, 1992).
[21] S. Leibler, J. Phys. (Paris) **47**, 507 (1986).
[22] S. Leibler and D. Andelman, J. Phys. (Paris) **48**, 2013 (1987).
[23] S. A. Safran, P. A. Pincus, and D. Andelman, Science **248**, 354 (1990).
[24] S. A. Safran, P. A. Pincus, D. Andelman, and F. C. MacKintosh, Phys. Rev. A **43**, 1071 (1991).
[25] D. Andelman, T. Kawakatsu, and K. Kawasaki, Europhys. Lett. **19**, 57 (1992).
[26] T. Kawakatsu, D. Andelman, K. Kawasaki, and T. Taniguchi, J. Phys. II **3**, 971 (1993).
[27] T. Taniguchi, K. Kawasaki, D. Andelman, and T. Kawakatsu, J. Phys. II **4**, 1333 (1994).
[28] R. Lipowsky, J. Phys. II **2**, 1825 (1992).
[29] F. Jülicher and R. Lipowsky, Phys. Rev. Lett. **70**, 2964 (1993).
[30] U. Seifert, Phys. Rev. Lett. **70**, 1335 (1993).
[31] F. C. MacKintosh and S. A. Safran, Phys. Rev. E **47**, 1180 (1993).
[32] J. L. Harden and F. C. MacKintosh, Europhys. Lett. **28**, 495 (1994).
[33] F. Jülicher and R. Lipowsky, Phys. Rev. E **53**, 2670 (1996).
[34] P. B. Sunil Kumar, G. Gompper, and R. H. Lipowsky, Phys. Rev. E **60**, 4610 (1999).
[35] W. T. Góźdź and G. Gompper, Europhys. Lett. **55**, 587 (2001).
[36] C. Gebhardt, H. Gruler, and E. Sackmann, Z. Naturforsch. C **32**, 581 (1977).
[37] J. A. F. O. den Kamp, Annu. Rev. Biochem. **48**, 47 (1979).
[38] A. J. Verklejj, R. F. A. Zwaal, B. Roelofsen, P. Comfurius, D. Kastelijn, and L. L. M. van Deenen, Biochim. Biophys. Acta **323**, 178 (1973).
[39] P. Sens and M. S. Turner, Biophys. J. **86**, 2049 (2004).
[40] T. R. Baekmark, G. Elender, D. D. Lasic, and E. Sackmann, Langmuir **11**, 3975 (1995).
[41] M. M. Kozlov and W. Helfrich, Langmuir **8**, 2792 (1995).
[42] J. M. Ziman, *Principles of the Theory of Solids* (Cambridge University Press, Cambridge, England 1972).
[43] F. Jülicher and U. Seifert, Phys. Rev. E **49**, 4728 (1994).
[44] L. Miao, U. Seifert, M. Wortis, and H. G. Döbereiner, Phys. Rev. E **49**, 5389 (1994).
[45] *Handbook of Mathematical Functions*, edited by M. Abramowitz and I. A. Stegun (Dover, New York, 1972).